Journal of Power Sources 191 (2009) 417–427

Contents lists available at ScienceDirect

Journal of Power Sources

journal homepage: www.elsevier.com/locate/jpowsour

Existence of the phase drainage diagram in proton exchange membrane fuel cell fibrous diffusion media

E.F. Medici*, J.S. Allen

Dept. of Mechanical Engineering - Engineering Mechanics, Michigan Technological University, Houghton, MI, 49931, United States

ARTICLE INFO

Article history:
Received 3 January 2009
Received in revised form 16 February 2009
Accepted 16 February 2009
Available online 3 March 2009

Keywords:
PEM fuel cell
Diffusion media layer
Viscous fingering
Capillary fingering
Stable displacement
Drainage phase diagram

ABSTRACT

It is well established that drainage in porous media can be characterized by two nondimensional numbers: the capillary number, *Ca*, and the viscosity ratio, *M*. Both quantities are useful to distinguish which force (viscous or capillary) is governing the fluid displacement behavior. This information is summarized in the *Ca*–*M* phase diagram. The *Ca*–*M* phase diagram is strongly dependent upon fluid properties and the porous medium morphology and wettability. Experimental evidence suggests that the morphology of the porous medium has an important role in the behavior in the fluid displacement. In this work, *Ca*–*M* phase diagram of fuel cell diffusion media layer (DM) is explored using a pseudo-Hele–Shaw experimental setup. This phase diagram will be explored together with the characteristic pressure curves of each displacement type. This *Ca*–*M* phase diagram will provide a fundamental resource for understanding the dynamics of the diffusion process and transport characteristics taking place inside of the DM as well as a characterization method for DMs.

1. Introduction

Drainage is the displacement of a wetting fluid by the injection of a nonwetting fluid. When drainage takes place a in porous media three types of fluid flow behavior can arise. One type of flow is originated when the injected fluid has lower viscosity than the displaced fluid. The injected fluid permeates irregularly through the porous material resulting in the formation of multiple conduits or fingers. This resulting flow distribution is characterized by fingers of approximately the same size and is called viscous fingering. The other two types of flow are created when the injected fluid has higher viscosity than the displaced fluid. If the injection flow rate is relatively slow, the injected fluid again generates irregular conduits within the porous media. The resulting flow distribution is characterized by the formation of a few fingers of different sizes and is called capillary fingering. If the injection flow rate is relatively high, the injected fluid permeates evenly through the porous media without finger formations; this resulting flow distribution is called stable displacement. Lenormand [1,2] presented a phase diagram that summarizes these three types of flow distribution in porous media in a single chart, called Drainage Phase Diagram, illustrated in Fig. 1. This phase diagram is based on two nondimensional parameters, the capillary number, *Ca*, and the viscosity ratio, *M*:

$$Ca = \frac{v\mu_{nw}}{\sigma} \quad (1)$$

$$M = \frac{\mu_{nw}}{\mu_{w}} \quad (2)$$

where v is the fluid velocity, μ_w and μ_{nw} are the wetting and nonwetting fluids viscosities, and σ is the surface tension.

These flow instabilities in porous media, viscous and capillary fingering, have been an object of study for a long time [3–5] and in diverse applications such as oil recovery [6], drug delivery [7], water transport in soil [8], among others; but it has been largely omitted from fuel cell research.

A typical proton exchange membrane (PEM) fuel cell consist of a series of porous layers compressed between bipolar plates. These layers, starting from the anode side, are the diffusion media layer, DM, (5–10 μm pore size and 150–400 μm thick), the micro-porous layer, MPL, (100–500 nm pore size and 10–20 μm thick), the catalyst layer or electrode (0.1–1 μm pore size and 5–30 μm thick), the proton exchange membrane (50–200 μm thick). These layers repeat on reverse order in the cathode side. Fig. 2 shows SEM images of a diffusion media layer at 100× magnification. These layers are generally treated with a polytetrafluoroethene (PTFE) coating making the pore surface hydrophobic.

The amount of water generated inside the fuel cell must be carefully controlled and distributed [9]. Remove too much water and the PEM begins to dry out, thereby decreasing proton transport. Remove too little water and it begins to accumulate, blocking the

* Corresponding author. Tel.: +1 906 487 4332; fax: +1 906 487 2822.
E-mail address: efmedici@mtu.edu (E.F. Medici).

0378-7753/$ – see front matter © 2009 Elsevier B.V. All rights reserved.
doi:10.1016/j.jpowsour.2009.02.050

Nomenclature

r	tube radius (cm)
v	fluid velocity ($m\,s^{-1}$)
q	volumetric flow rate ($ml\,s^{-1}$)
t	time (s)
σ	surface tension ($N\,m^{-1}$)
μ_w	wetting fluid viscosity (Pa s)
μ_{nw}	nonwetting fluid viscosity (Pa s)
P	pressure (kPa)
A	wetted area (cm^2)
S	fluid–fluid interface length (cm)
L	length of the sample (cm)
H	width of the sample (cm)
Ca	capillary number
M	viscosity ratio
PEM	proton exchange membrane
PTFE	polytetrafluoroethene
DM	diffusion media
MPL	micro-porous layer
PDMS	polydimethylsiloxane
SEM	scanning electron microscope
CCD	charge coupled device
CMOS	complementary metal oxide semiconductor

access of the reactants to the catalyst layer which stops the chemical reaction and reduces the cell efficiency. Also, water accumulation may locally prevent the flow of reactants through the bipolar plate channels, reducing the chemical reaction rate upstream and increasing the degradation of the fuel cell components.

Thus, water management is critical to reliable PEM fuel cell operation. There have been a numerous studies to improve the water management in PEM fuel cells including: external humidification [10], size and profile of the bi-polar plates channels [11], thickness and porosity of the layers [12,13], the addition of the MPL [14], wettability of the layers [15], among others.

Experimental evidence suggests that the water distribution inside of the DM is not uniform and water is transported in a fingering-type flow. Litster et al. [16] present evidence of the fingering type of pattern using fluorescence microscopy. In their experiment, distilled water with fluorescence dye was injected into a DM from the bottom surface, obtaining a "through plane" percolation. Also, evidence of nonuniform water distribution was found using magnetic resonance imaging by Tsushima et al. [17], as well as neutron imaging by Satija et al. [18]. Sinha et al. [19], using a simple calculations for the water generated in a fuel cell under normal operating conditions and the drainage phase diagram, suggested that the main regime expected in a fuel cell is capillary fingering. In this calculation, the effect of different pore size along the different layers was not taken into account. Kimball et al. [20] suggest that water will flow along the DM only through the largest pores, but they omit the effect of the MPL in their discussion. Despite all this evidence of capillary driven flow, there has not been a fundamental study of capillarity and drainage flow patterns on fuel cell water management.

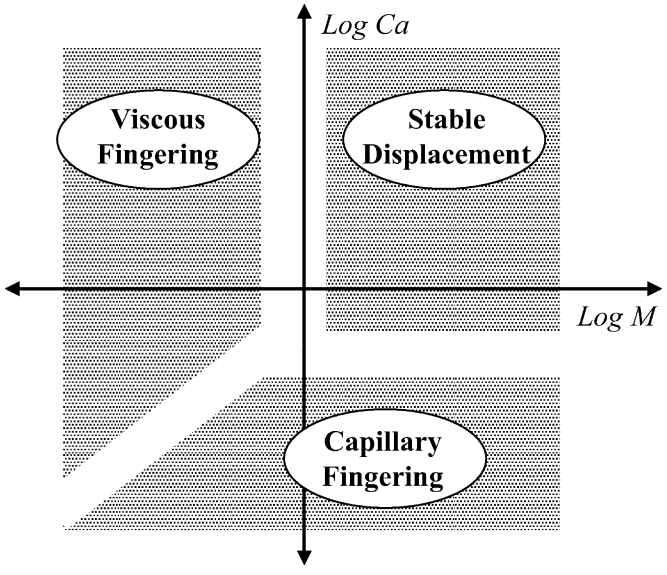

Fig. 1. Drainage phase diagram.

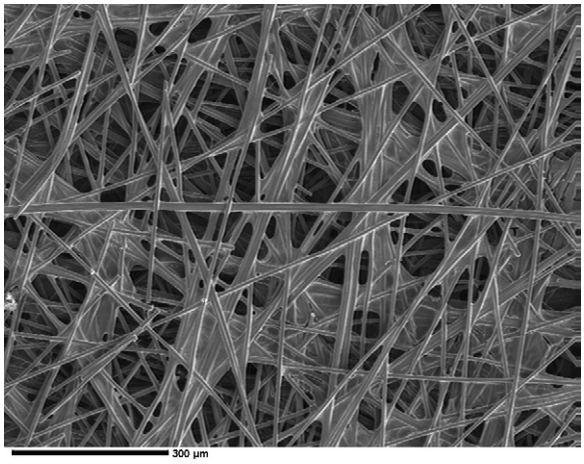

Fig. 2. SEM image of the Toray T060 DM layer under study, 100×magnification.

The objective of this study is to explore the three types of drainage flow in DM separately and gain knowledge of the water behavior inside of the DM which may occur during the operation of the fuel cell. The understanding of these basic mechanisms will be useful for developing reliable robust water management strategies in low temperature fuel cells.

2. Experimental setup

The diffusion media used for this study is Toray T060 with a pore size distribution in the range of 5–10 μm and a 7% by weight Teflon treatment. Fig. 2 shows an SEM image of the sample used at 100× magnification. This 5 cm × 5 cm × 0.02 cm sample is placed in a cell between two layers of polydimethylsiloxane (PDMS). PDMS is a transparent, compliant, and hydrophobic silicon material used to seal the top and bottom surfaces of the diffusion media ensuring water percolation within the diffusion media while maintaining visual access. Fig. 3 illustrates the PDMS-DM-PDMS cross-section, which is referred to as a pseudo-Hele–Shaw cell. To prevent filtration between the PDMS and the DM surfaces, the cell layers were compressed between two pieces of Plexiglas ™ surrounded by a metallic frame which was held in place by four screws. The screws were adjusted to produce a 20 kPa compression pressure over the test sample, which generates a 0.05% strain deformation (0.1 μm compression). Four springs were also placed between the frames in order to obtain uniform compression along the cell.

A Kulite XCS062100 differential pressure transducer located in the inlet tubing was used to measure the percolation pressure. The pressure was recorded using a Keithley 2700 digital multimeter at

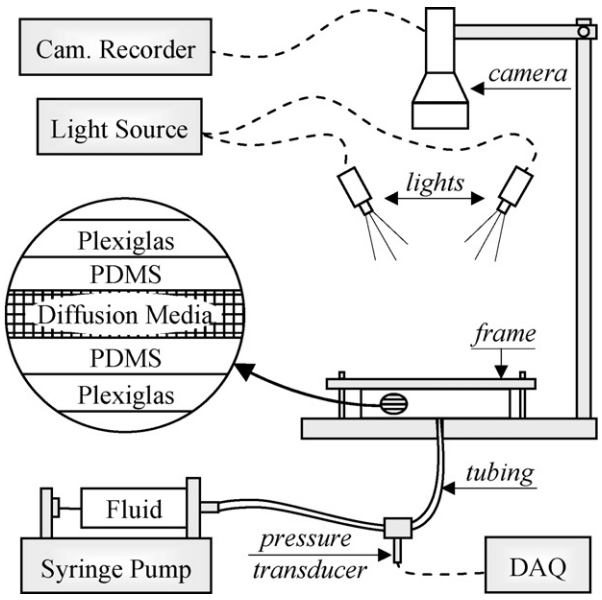

Fig. 3. Experimental setup details.

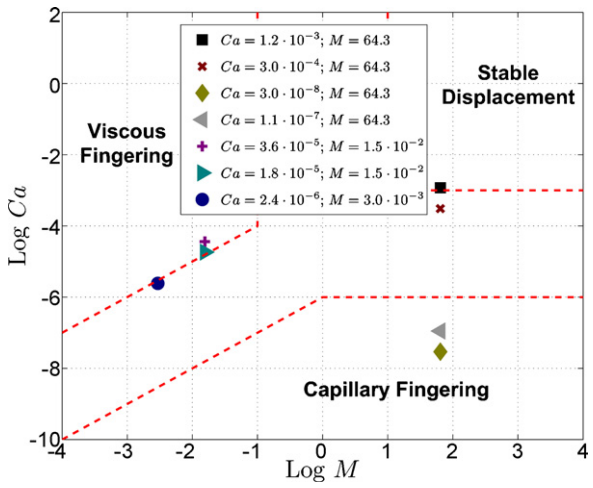

Fig. 4. Points in the drainage phase diagram explored experimentally. Dashed lines represent the hypothetical limits for each flow regime.

intervals of 0.1 s. A camera located at 0.5 m from the cell was used to collect images of the drainage during the experiment. Due to the different time scales of the experiments, two types of camera were used. A Panasonic GP-KS125 CCD camera was used for the capillary fingering set of experiments, while a high speed Photron Fastcam-Ultima APX-RS CMOS camera was used for the stable displacement and viscous fingering set of experiments. In order to have enough contrast between the injected and the displaced fluid in the DM and to avoid camera self-reflection from the cell, a diffusive illumination system was used. The working fluid was injected through a 2 mm diameter hole located in the middle of the bottom PDMS layer using a syringe pump at a constant flow rate. Two different syringe pumps were used. An ultra-low flow rate syringe pump, Harvard Apparatus model 2274, was used for the capillary fingering set of experiments, while a Harvard Apparatus model 938 syringe pump was used for the stable displacement and viscous fingering set of experiments. The flow rate and the working fluid could be varied in order to explore different points in the drainage phase diagram. The flow rate was changed to set different capillary numbers and the working fluid was changed to set different viscosity ratios. A reference capillary number, *Ca*, for each experiment was calculated at the inlet using Eq. (1), where the inlet velocity v was calculated as $v = q/\pi r^2$, where q is the volumetric flow rate and r is the radius of the inlet tube. The reference viscosity ratio, *M*, for each experiment was calculated using Eq. (2), where the terms wetting and nonwetting fluid refer to the displaced and injected fluids, respectively. Table 1 summarizes the flow rates, working fluids, capillary number, among other technical data used during each experiment.

Table 1
Test conditions for each experiment.

Regime	Injected/ displaced	*M*	q (ml s^{-1})	*Ca*	Frame rate (fps)
SD	Water/air	64	0.228	1.2×10^{-3}	60
SD	Water/air	64	0.059	3.0×10^{-4}	250
CF	Water/air	64	2.1×10^{-5}	1.1×10^{-7}	0.06
CF	Water/air	64	5.6×10^{-6}	3.0×10^{-8}	0.05
VF	Air/water	1.5×10^{-2}	0.5	3.6×10^{-5}	500
VF	Air/water	1.5×10^{-2}	0.228	1.8×10^{-5}	500
VF	Water/oil	3×10^{-3}	2.5×10^{-4}	2.4×10^{-6}	–

SD: stable displacement; CF: capillary fingering; VF: viscous fingering.

The test sample was placed in a desiccator for approximately 24 h prior to each experiment run.

Three different sets of experiments, designed to explore each of the three possible fluid behaviors shown on the drainage phase diagram, were performed. In the stable displacement experiments, air was displaced from the DM by injecting water at a high flow rate. During the capillary fingering experiments, air was displaced from the DM by injecting water at a low flow rate. In the viscous fingering experiments, water was displaced from the DM by injecting air or oil was at a high flow rate. Fig. 4 shows the capillary number, *Ca*, and viscosity ratio, *M*, of each experiment in the drainage phase diagram.

From the experiments, the top view images of the percolation evolution and the percolation pressure curve were recorded in parallel. The images from the CCD camera were collected using EPIX PIXCI imaging board and XCAP frame grabber, while the images from the CMOS camera were collected using Fastcam Viewer software. From these images, the percentage of the total area occupied by the injected fluid and the interface of injected–displaced fluids were calculated for each test. The time evolution of the occupied area is referred to as a saturation curve, while the time evolution of the fluid–fluid interface is refereed to as a front length curve. To obtain these saturation and front length curves, an image post-processing analysis was performed.

2.1. Image post-processing

The procedure to obtain the fluid–fluid interface began by transforming the collected images to gray scale. A background reference image of the DM before the percolation started was subtracted from each image. By applying a threshold value to the difference between actual and reference pictures, the location of injected and displaced fluids can be easily identified. The interface between the injected and displaced fluids was captured using an edge detection algorithm written in Matlab. The interface was reconstructed by plotting the border points, indicated by the line superimposed on Fig. 5 for stable displacement, Fig. 9 for capillary fingering, and Fig. 13 for viscous fingering.

The area saturated with injected fluid from the top view is referred as the wetted area, and is denoted as *A*. The interface line between the injected and displaced fluid is referred to hereafter as the front length, *S*. Using the described technique, the wetted area, *A*, and the front length, *S*, were calculated at each time interval. The front length and the wetted area were nondimensionalized

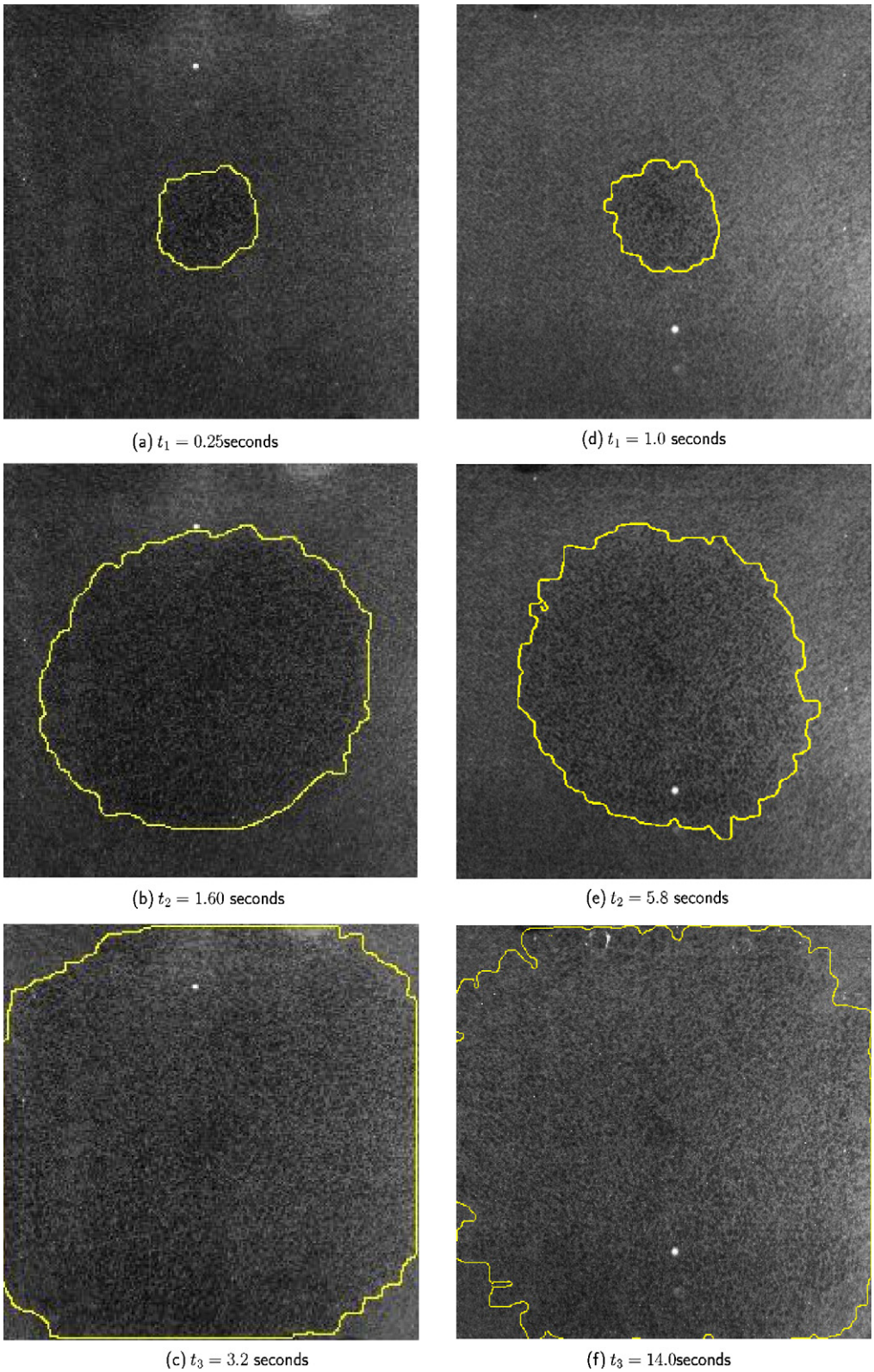

(a) $t_1 = 0.25$seconds

(d) $t_1 = 1.0$ seconds

(b) $t_2 = 1.60$ seconds

(e) $t_2 = 5.8$ seconds

(c) $t_3 = 3.2$ seconds

(f) $t_3 = 14.0$seconds

Fig. 5. Three stages of the water–air percolation evolution for the two stable displacement flow regime experiments. Yellow lines identify the water–air interface. Water is inside and air is outside of region defined by the interface line. Right column images: time evolution for experiment at 0.228 ml s^{-1}($Ca = 1.2 \times 10^{-3}$). Left column of images: time evolution for experiment at 0.059 ml s^{-1} ($Ca = 3.0 \times 10^{-4}$).

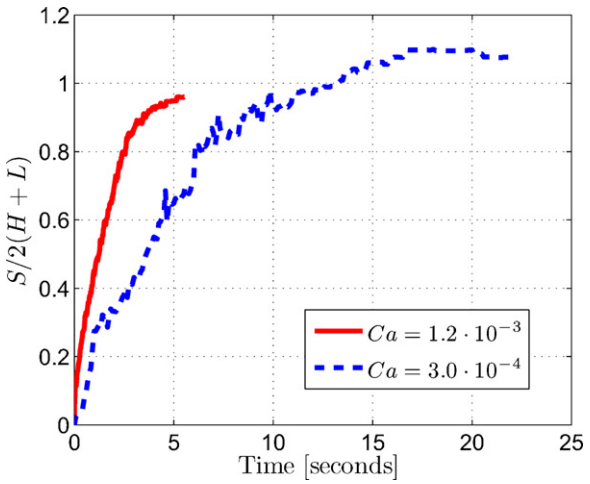

Fig. 6. Nondimensional front length curves for the two stable displacement flow regime experiments. These nondimensional front lengths curves were calculated from the time evolution images of water–air interface. Experiments were performed injecting water and displacing air ($M = 64$) at different injection flow rate of 0.228 and 0.059 ml s^{-1} which correspond to $Ca = 1.2 \times 10^{-3}$ and $Ca = 3.0 \times 10^{-4}$, respectively.

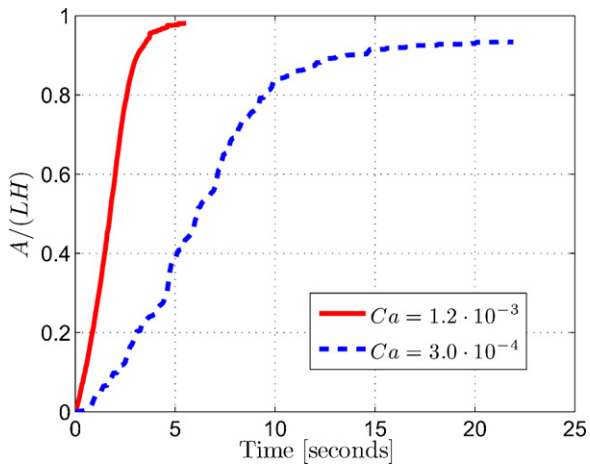

Fig. 7. Nondimensional wetted area curves for the two stable displacement flow regime experiments. These nondimensional wetted areas curves were calculated from the time evolution images of water–air interface. Experiments were performed injecting water and displacing air ($M = 64$) at different injection flow rate of 0.228 and 0.059 ml s^{-1} which correspond to $Ca = 1.2 \times 10^{-3}$ and $Ca = 3.0 \times 10^{-4}$, respectively.

using the length and width of the test sample, L and H, respectively. The front length is nondimensionalized by the perimeter of the test sample $2(L + H)$ and the wetted area is nondimensionalized by the projected area of the test sample $L \times H$.

3. Observations

3.1. Stable displacement

When the injection flow rate is high enough to have a Ca number greater than 10^{-3} and the viscosity ratio between the injected and displaced fluids is greater than one, the drainage flow regime is stable displacement. The stable displacement flow regime is characterized by a flow pattern where all pores sizes are filled. Starting from the center injection hole, the injected fluid will fill all the pores until it reaches the edge of the test sample and the experiment ends. The interface between injected and displaced fluids can be assumed as a circular line shape (from a top view) concentric to the injection hole. In this stable displacement set of experiments, air was displaced by injecting water (viscosity ratio of $M = 64$). The flow rates used were 0.228 and 0.059 ml s^{-1} which results in a Ca of 1.2×10^{-3} and 3.0×10^{-4}, respectively. Images were collected using the CMOS camera at 60 and 250 fps, respectively. Three stages of the water percolation evolution for the two injection flow rates are shown in Fig. 5. These figures include the interface line between the injected and displaced fluids.

From the experiment images, the front length S and wetted area A curves were calculated for each image. The nondimensional front length curves, Fig. 6, and the nondimensional wetted area curves, Fig. 7, reach a peak value and then plateau after an initial transient period. The lower Ca experiment has the lower steady wetted area (lower saturation level) and the higher steady front length. The steady front length is greater than one which can be explained using the phase diagram. Due to the proximity to the transition region between the stable displacement and capillary fingering, the uniform shape of stable displacement begins to develop small capillary fingers. This effect can be seen in Fig. 5(f). The presence of these fingers reduces the level of saturation, increases the interface front length, and increases the time to reach saturation.

The corners of the cell will never be wetted and saturation level will be always lower than one because the injected fluid spreads circular until it reaches the edges of the test sample (it will reach the middle of all the side edges at approximately the time) and the experiments ends.

The pressure drop during percolation exhibits an gradual growth as water is injected, shown in Fig. 8. Additional pressure is required to inject more water in order to displace the previously injected water. Also, the greater the capillary number the higher the fluid velocity and the larger the required pressure drop.

3.2. Capillary fingering

The capillary fingering drainage flow regime is characterized by a very slow injection flow rate and therefore a very small Ca. This slow flow rate allows the injected fluid to reach a quasi-steady capillary equilibrium. Starting from the injection hole, the injected fluid will percolate only through the pores that offer the smallest capillary resistance. These low capillary resistant pores are the largest pores or the pores with small internal contact angle [21]. This type of fluid flow no longer has the uniform circular shape obtained in stable displacement flow regime. On the contrary, this flow pattern

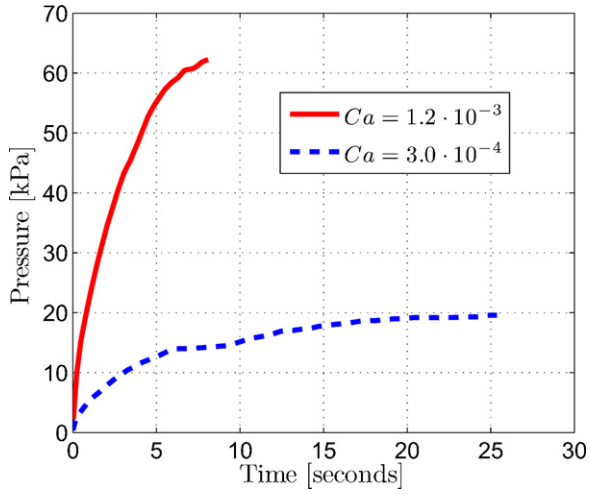

Fig. 8. Percolation pressure curves for the two stable displacement flow regime experiments. Experiments were performed by injecting water and displacing air ($M = 64$) at different injection flow rate of 0.228 and 0.059 ml s^{-1} which corresponds to $Ca = 1.2 \times 10^{-3}$ and $Ca = 3.0 \times 10^{-4}$, respectively.

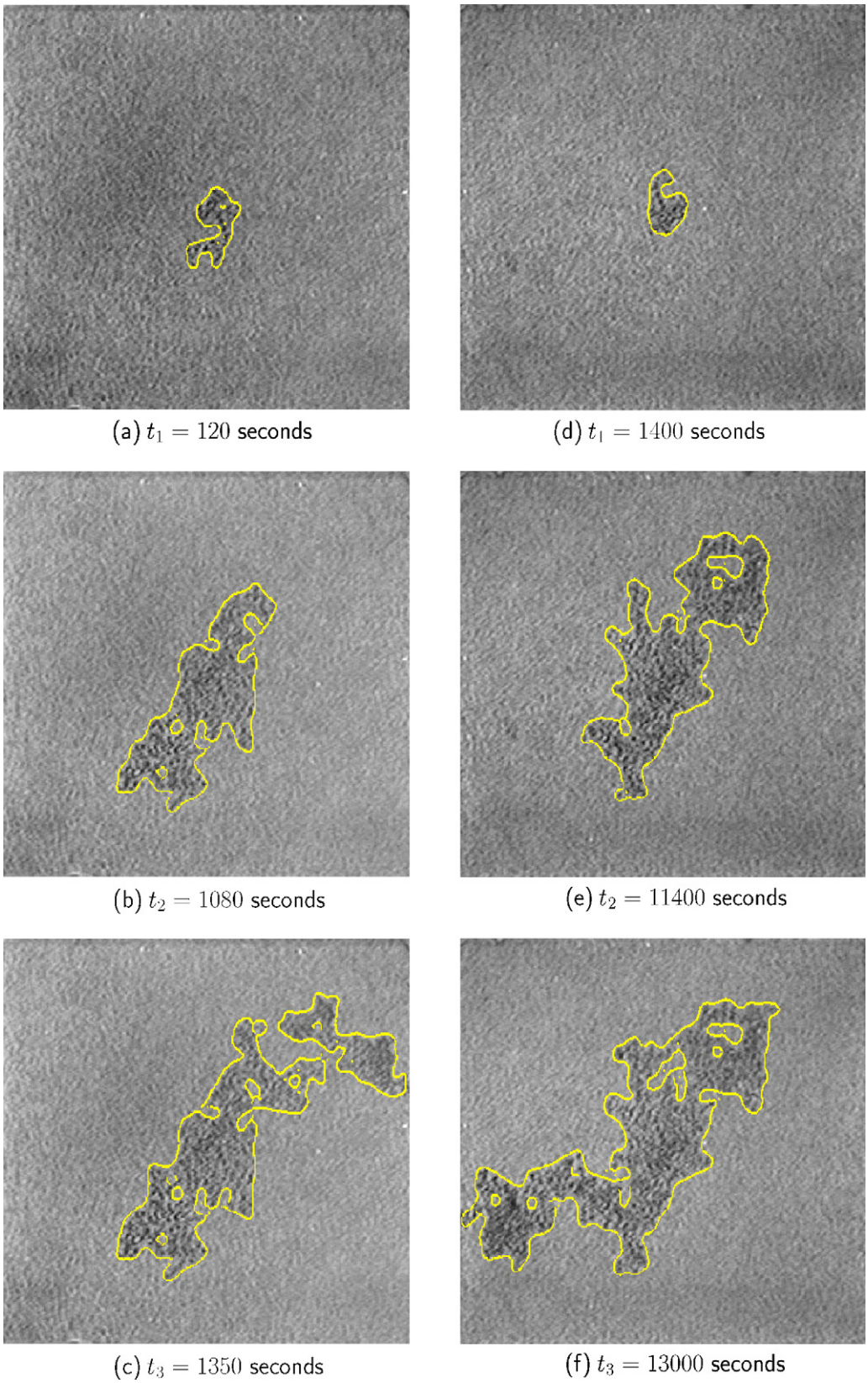

Fig. 9. Three stages of the water–air percolation evolution for the two capillary fingering flow regime experiments. Yellow lines identify the water–air interface. Water is inside and air is outside of region defined by the interface line. Right column images: time evolution for experiment at 2.1×10^{-5} ml s^{-1} ($Ca = 1.1 \times 10^{-7}$). Left column of images: time evolution for experiment at 5.6×10^{-6} ml s^{-1} ($Ca = 3.0 \times 10^{-8}$).

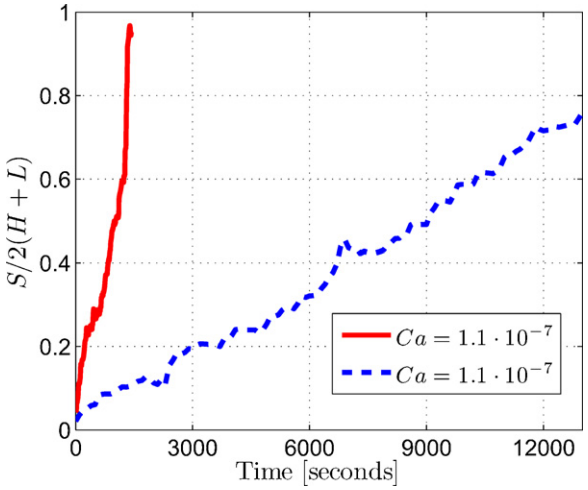

Fig. 10. Nondimensional front length curves for the two capillary fingering flow regime experiments. These nondimensional front lengths curves were calculated from the time evolution images of water–air interface. Experiments were performed injecting water and displacing air ($M = 64$) at different injection flow rate of 2.1×10^{-5} and 5.6×10^{-6} ml s^{-1} which correspond to $Ca = 1.1 \times 10^{-7}$ and $Ca = 3.0 \times 10^{-8}$, respectively.

is characterized by the formation few irregular conduits or fingers through the porous media. The experiment ends when the injected fluid reaches one of the edges of the test sample.

During this capillary fingering set of experiments, air was displaced by injecting water (viscosity ratio of $M = 64$). The flow rates used were 2.1×10^{-5} and 5.6×10^{-6} ml s^{-1} which results in a Ca of 1.1×10^{-7} and 3.0×10^{-8}, respectively. In order to achieve these flow rates, an ultra-low flow rate syringe pump, Harvard Apparatus model 2274, was used. Images were collected using the CCD camera at 0.06 and 0.05 fps, respectively. Three stages of the water percolation evolution for the two different injection flow rates are shown in Fig. 9. These figures include the interface line between the injected and displaced fluids.

From the experiment images, front length S and the wetted area A curves were calculated. The capillary fingering regime is characterized by incomplete saturation of the media. Therefore, the nondimensional front length curves, Fig. 10, and the nondimensional wetted area curves, Fig. 11, show a lower saturation level when compared to the stable displacement saturation level.

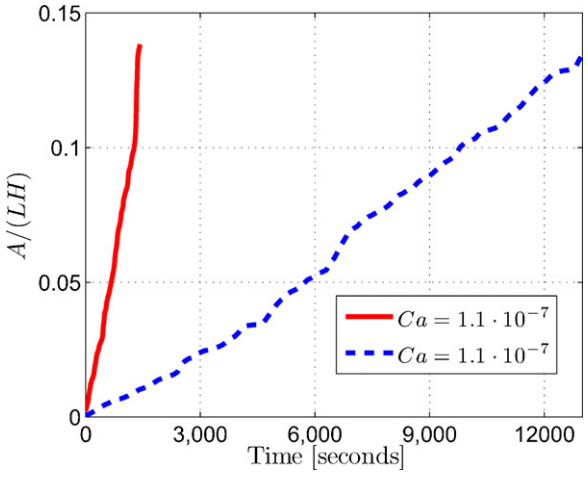

Fig. 11. Nondimensional wetted area curves for the two capillary fingering flow regime experiments. These nondimensional wetted areas curves were calculated from the time evolution images of water–air interface. Experiments were performed injecting water and displacing air ($M = 64$) at different injection flow rate of 2.1×10^{-5} and 5.6×10^{-6} ml s^{-1} which correspond to $Ca = 1.1 \times 10^{-7}$ and $Ca = 3.0 \times 10^{-8}$, respectively.

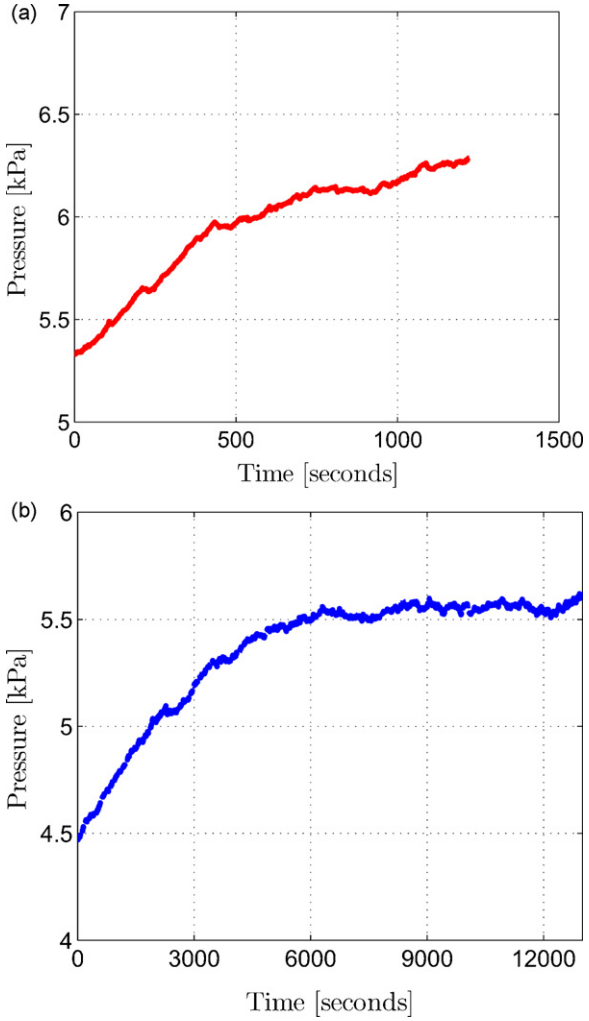

Fig. 12. Percolation pressure curves for the two capillary fingering flow regime experiments. Experiments were performed by injecting water and displacing air ($M = 64$) at different injection flow rate of 2.1×10^{-5} and 5.6×10^{-6} ml s^{-1} which correspond to $Ca = 1.1 \times 10^{-7}$, (a), and $Ca = 3.0 \times 10^{-8}$, (b), respectively.

In the capillary fingering regime, the percolation pressure has an initial gradual growth which levels off to a constant pressure as water is injected. When the pressure in the syringe is higher than the capillary pressure in the DM, the water–air interface moves (meniscus displacement). However, due to the low flow rate, there is not enough volume of water to keep the meniscus moving continuously and the interface motion stops. Percolation subsides until the system reaches a quasi-steady equilibrium and the pressure in the syringe pump exceeds the capillary pressure. Thus, the pressure curve oscillates around the capillary pressure, as seen in Fig. 12(b).

As the Ca increases, less time is required for the water to reach one of the edges. At the higher Ca, the flow regime approaches the intermediate region between stable displacement and capillary fingering, the quasi-steady capillary equilibrium displacement is no longer achieved and the pressure continuously increases during the percolation as shown in Fig. 12(a). The increased fluid velocity results in an increased initial pressure at which the percolation begins. The initial pressure was 5.3 ± 0.35 kPa for $Ca = 1.1 \times 10^{-7}$ while for $Ca = 3.0 \times 10^{-8}$ and the initial pressure was 4.5 ± 0.35 kPa.

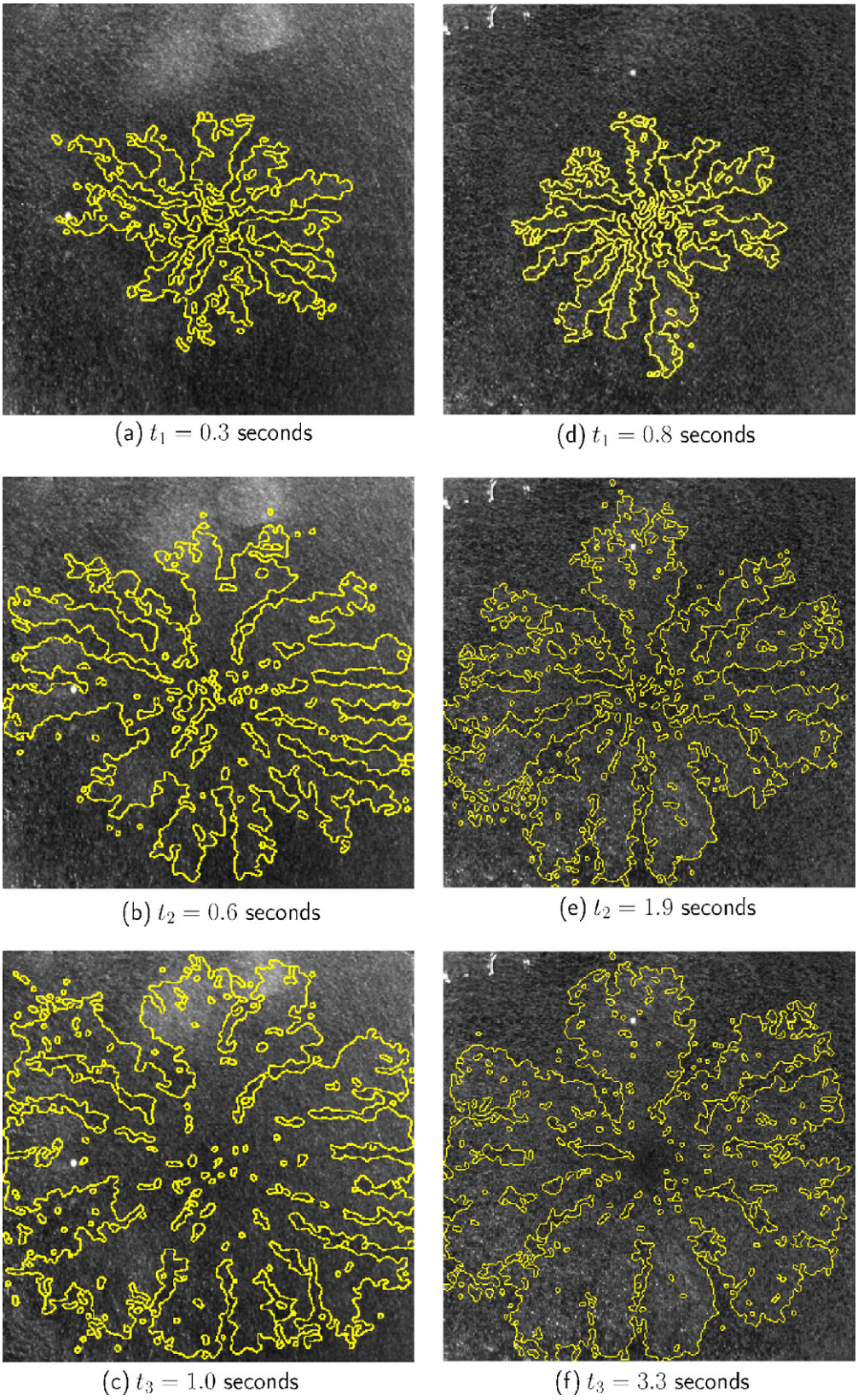

Fig. 13. Three stages of the air–water percolation evolution for the two viscous fingering flow regime experiments. Yellow lines identify the air–water interface ($M = 1.5 \times 10^{-2}$). Air is inside and water is outside of region defined by the interface line. Right column images: time evolution for experiment at 0.5 ml s^{-1} ($Ca = 3.6 \times 10^{-5}$). Left column of images: time evolution for experiment at 0.228 ml s^{-1} ($Ca = 1.8 \times 10^{-5}$).

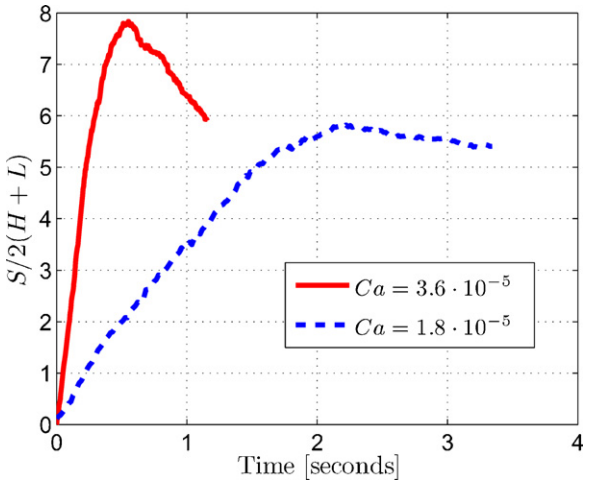

Fig. 14. Nondimensional front length curves for the two viscous fingering flow regime experiments. These nondimensional front lengths curves were calculated from the time evolution images of air–water interface. Experiments were performed injecting air and displacing water ($M = 1.5 \times 10^{-2}$) at different injection flow rate of 0.5 and 0.228 ml s^{-1} which correspond to $Ca = 3.6 \times 10^{-5}$ and $Ca = 1.8 \times 10^{-5}$, respectively.

3.3. Viscous fingering

When the injected fluid has lower viscosity than the displaced fluid, the drainage flow regime is viscous fingering. Due to the low viscosity of the injected fluid the percolation pressure continuously decreases until the injected fluid reaches the edge of the test sample. The pressure levels off to a minimum value and the experiment stops. The resulting flow patterns is characterized by the formation of multiple fingers of approximately the same size. In this set of experiments, the DM was originally saturated with water and air was injected to displace the water ($M = 1.5 \times 10^{-2}$). The flow rates used were 0.5 and 0.228 ml s^{-1} which results in a Ca of 3.6×10^{-5} and 1.8×10^{-5}, respectively. Images were collected using the CMOS camera at 500 fps for both flow rates. Three stages of the air percolation evolution for the two different injection flow rates are shown in Fig. 13. These figures include the interface line between the injected and displaced fluids.

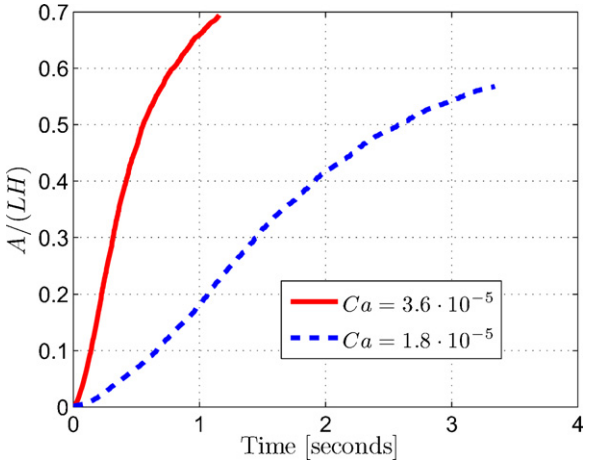

Fig. 15. Nondimensional wetted area curves for the two viscous fingering flow regime experiments. These nondimensional wetted areas curves were calculated from the time evolution images of air–water interface. Experiments were performed injecting air and displacing water ($M = 1.5 \times 10^{-2}$) at different injection flow rate of 0.5 and 0.228 ml s^{-1} which correspond to $Ca = 3.6 \times 10^{-5}$ and $Ca = 1.8 \times 10^{-5}$, respectively.

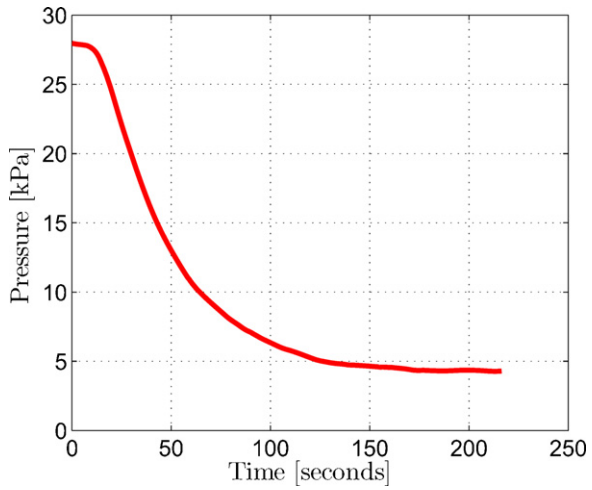

Fig. 16. Percolation pressure curve for the viscous fingering flow regime experiment. Experiment was performed by injecting water and displacing SAE 30 motor oil ($M = 3 \times 10^{-3}$) at flow rate of 2.5×10^{-4} which correspond to $Ca = 2.4 \times 10^{-6}$.

From the experiment images, the front length S and the wetted area A curves were calculated. The nondimensional front lengths curves, shown in Fig. 14, have a maximum larger than one due to the presence of many fingers when compared with stable displacement and capillary fingering. For Ca of 3.6×10^{-5} the maximum S was 5.8 and for $Ca = 1.8 \times 10^{-5}$ the maximum S was 7.8. As the DM is filled, these fingers coalescence into wider conduits and the front lengths slowly decay over a period of time. However, the nondimensional wetted area curves are characterized by incomplete saturation of the media as shown in Fig. 15.

During viscous fingering regime, the combination of the small pore size of the DM and the relative high viscosity of the water, as compared with air, displacement of the water requires high pressures which compresses the air inside the injection tubing. At the onset of percolation, the compressed air expands rapidly through the DM originating a fast growth of the fingers. Subsequently, the growth speed of the fingers does not correspond to the injection flow rate. The percolation pressure curves include the rapid release of stored energy in the compressed air and this behavior does not correspond to drainage viscous fingering flow regime. Therefore, the air–water percolation pressure curves are not presented.

In order to avoid this problem and to keep a small viscosity ratio, an experiment using incompressible fluids was performed. In this experiment the DM was originally saturated with SAE 30 motor oil and it was displaced by injecting water (viscosity ratio of $M = 3 \times 10^{-3}$). The flow rate used in this experiment was 2.5×10^{-4} ml s^{-1} which results in a Ca of 2.4×10^{-6}. Due to the low contrast between the water and the oil in the DM, it was not possible to identify the fluid–fluid interface. Only the pressure drop is presented, see Fig. 16. When the water is injected and the oil displaced the overall viscous forces are reduced and therefore the pressure drop shows a gradual decay as the water is injected. When the fingers reach the edges the pressure levels off to the minimum value as was expected and the experiment ends.

4. Discussion

Previous publications on the study of the transport mechanisms of the water through the DM were focused on ex situ experiments where the injected fluid is forced to cross the thickness of the DM for "through-plane" percolation. These ex situ experiments are mimicking the operating conditions of a real fuel cell. In this paper the fluid is injected on a small area on one side of the DM, forcing it to percolate along the DM for "in-plane" percolation.

The advantages of "in-plane" over "through-plane" is that the percolation occurs over a longer time which increases the experiment precision, especially in the measurement of the percolation pressure. While "in-plane" experiments tend to be more realistic to the fuel cell operating conditions, the "through-plane" has the advantages of higher visual area and longer experimental time which are essential for a more fundamental understanding of transport mechanisms.

Benzinger et al. [22] measured the pressure required for the water to cross along the DM. Based on their experiment, water will cross along the DM at approximately 5.3 kPa. This pressure value can be compared to the initial value in the pressure curves for capillary fingering regime (4.5 and 5.3 kPa) shown in Fig. 12(a) and (b). The data from Benzinger et al. [22] represents only one point of the characteristic pressure for the capillary fingering flow region of the drainage phase diagram and cannot provide visual access to identify the fingering pattern.

Litster et al. [16] used an experimental setup where water with fluorescence dye was injected along the bottom surface generating a "through-plane" percolation. Under this arrangement, their experimental setup is a realistic approximation of the operating conditions of a fuel cell. However, the time and the space where the fingers take place are small and hard to characterize. In this setup it would be difficult to distinguish between the different drainage flow regimes.

4.1. Drainage flow regimes in DMs

All three flows patterns can occur during PEM fuel cell operation. Each flow pattern has its own characteristic. The most immediate and easy to discern characteristic is the pattern shape: uniform, a few narrow fingers, or multiple fingers. Associated with these shapes are the wetted area curves and the front length curves. Also, each flow pattern will have a unique percolation pressure and time scale which can vary from seconds for viscous fingering and stable displacement to hours for capillary fingering. All these characteristics combined together can be used to classify different diffusion media according to their susceptibility to each drainage flow pattern.

It is also important to identify which conditions will trigger each flow regime, especially capillary fingering and stable displacement. When the a particular flow regime in a porous media changes from capillary fingering to stable displacement the media will start to flood. The transition between stable displacement and viscous fingering will rarely occur in a fuel cell. Nevertheless, when there is pressure difference between the air channels (e.g. a water plug blocking the channel) and if this pressure is higher than the capillary pressure then the reactants will displace the water in a viscous fingering mode. To understand when this condition can be triggered, a closer look of the morphology of each porous layer in a PEM fuel cell is required.

Assuming a typical fuel cell of 1 kW and 1 m^2 active area operating for 1 h, 0.5 l of water will theoretically be produced [23]. The capillary number for this flow rate $q = 1.4 \times 10^{-1}$ ml s^{-1} is approximately $Ca = 5 \times 10^{-9}$ which corresponds to the capillary fingering flow regime. However, in a typical fuel cell assembly, a microporous layer (MPL) is located between the catalyst layer and the gas diffusion media. The cathode and anode MPLs, with a typical pore size in the order of 100–500 nm, increase the capillary force up to approximately 100–1000 times when compared with the capillary force on DM. As a consequence of this high capillary pressure in the MPL, the catalyst layers and the PEM are forced to operate under complete saturation conditions, keeping them hydrated [14]. In contrast, the capillary number for anode and cathode DMs (with pore size in the order of 5–10 μm) is lower resulting in a capillary fingering mode. This could be a desirable effect in the DM because during capillary fingering regime the fingers will allow the water reach the channel without flooding the DM.

5. Conclusions

An experimental setup was developed to have visual access of fuel cell diffusion media layer (DM) during percolation. The characteristic nondimensional numbers were varied in order to obtain the three different types of fluid flow behaviors specified in the drainage phase diagram. The nondimensional numbers were set by adjusting the injection flow rate as well as changing the working fluids. During the experiment, injection pressure was measured and the time-dependent water distribution was recorded. From the time dependent wetted area and front length as well as from the injection pressure it can be concluded that a change in the injection condition can completely change the water transport mechanism occurring in the DM. These changes can be associated with three different types of fluid flow behaviors, the stable displacement, the viscous fingering, and the capillary fingering. These three flow regimes summarize the expected transport mechanisms taking place in the DM during operation of fuel cells.

The results obtained in this paper not only support but also bring together the transport mechanism based on the capillary phenomena described by Litster et al. [16] and the pressure readings obtained by Benzinger et al. [22]. This experimental setup can be further developed to be used as a standard for characterizing DM as well as studying degradation mechanisms, compression effect on the percolation, durability, etc.

This work shows the importance of drainage transport mechanisms which are crucial for developing a consistent model of the PEM fuel cell. These transport mechanisms are not accounted for in current transport models of PEM fuel cell, but they can result in considerable differences in estimated amounts and distributions of water in fuel cells. These transport mechanisms should be incorporated into models capable of capturing two phase flow and capillarity. Finally, the *Ca–M* phase diagram provides a fundamental resource for characterization of fuel cell diffusion media.

Acknowledgments

This work was partially funded by DOE contract DE-FG36-07GO17018. The authors thank General Motors for providing the fuel cell diffusion media.

References

[1] R. Lenormand, E. Touboul, C. Zarcone, Journal of Fluid Mechanics 189 (1988) 165–187.
[2] R. Lenormand, Journal of Physics-Condensed Matter 2 (1990) SA79–SA88.
[3] G. Homsy, Annual Reviews in Fluid Mechanics 19 (1) (1987) 271–311.
[4] P. Adler, H. Brenner, Annual Reviews in Fluid Mechanics 20 (1) (1988) 35–59.
[5] P. King, Journal of Physics A 20 (1987) 529–534.
[6] L. Lake, Enhanced Oil Recovery, Prentice Hall, Inc., Old Tappan, NJ, 1989.
[7] A. Stephanou, S.R. McDougall, A.R.A. Anderson, M.A.J. Chaplain, J.A. Sherratt, Mathematical and Computer Modelling 41 (10) (2005) 1137–1156.
[8] J.L. Nieber, T.W.J. Bauters, T.S. Steenhuis, J.Y. Parlange, Journal of Hydrology 231 (2000) 295–307.
[9] H. Li, Y. Tang, Z. Wang, Z. Shi, S. Wu, D. Song, J. Zhang, K. Fatih, J. Zhang, H. Wang, Z. Liu, R. Abouatallah, A. Mazza, Journal of Power Sources 178 (1) (2008) 103–117.
[10] T.J.P. Freire, E.R. Gonzalez, Journal of Electroanalytical Chemistry 503 (1–2) (2001) 57–68.
[11] X. Li, I. Sabir, International Journal of Hydrogen Energy 30 (4) (2005) 359–371.
[12] C.S. Kong, D.-Y. Kim, H.-K. Lee, Y.-G. Shul, T.-H. Lee, Journal of Power Sources 108 (1–2) (2002) 185–191.
[13] U. Pasaogullari, C.-Y. Wang, Electrochimica Acta 49 (25) (2004) 4359–4369.
[14] Z. Qi, A. Kaufman, Journal of Power Sources 109 (1) (2002) 38–46.
[15] L. Giorgi, E. Antolini, A. Pozio, E. Passalacqua, Electrochimica Acta 43 (24) (1998) 3675–3680.
[16] S. Litster, D. Sinton, N. Djilali, Journal of Power Sources 154 (1) (2006) 95–105.
[17] S. Tsushima, K. Teranishi, K. Nishida, S. Hirai, Magnetic Resonance Imaging 23 (2) (2005) 255–258.

[18] R. Satija, D.L. Jacobson, M. Arif, S.A. Werner, Journal of Power Sources 129 (2) (2004) 238–245.
[19] P.K. Sinha, P.P. Mukherjee, C.Y. Wang, Journal of Materials Chemistry 17 (30) (2007) 3089–3103.
[20] E. Kimball, T. Whitaker, Y.G. Kevrekidis, J.B. Benzinger, AIChE Journal 54 (5) (2008) 1313–1332.
[21] V. Gurau, M.J. Bluemle, E.S.D. Castro, Y.-M. Tsou, J.A. Mann, T.A. Zawodzinski Jr., Journal of Power Sources 160 (2) (2006) 1156–1162.
[22] J. Benziger, J. Nehlsen, D. Blackwell, T. Brennan, J. Itescu, Journal of Membrane Science 261 (1–2) (2005) 98–106.
[23] L. James, D. Andrew, Fuel Cell Systems Explained, Wiley, Chichester–West Sussex–New York, 2000.